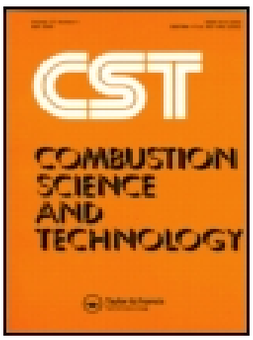

Combustion Science and Technology

ISSN: 0010-2202 (Print) 1563-521X (Online) Journal homepage: https://www.tandfonline.com/loi/gcst20

Comparison of Finite Rate Chemistry and Flamelet/Progress-Variable Models: Sandia Flames and the Effect of Differential Diffusion

Suo Yang, Xingjian Wang, Wenting Sun & Vigor Yang

To cite this article: Suo Yang, Xingjian Wang, Wenting Sun & Vigor Yang (2020): Comparison of Finite Rate Chemistry and Flamelet/Progress-Variable Models: Sandia Flames and the Effect of Differential Diffusion, Combustion Science and Technology, DOI: 10.1080/00102202.2020.1754809

To link to this article: https://doi.org/10.1080/00102202.2020.1754809

COMBUSTION SCIENCE AND TECHNOLOGY
https://doi.org/10.1080/00102202.2020.1754809

Taylor & Francis
Taylor & Francis Group

Comparison of Finite Rate Chemistry and Flamelet/Progress-Variable Models: Sandia Flames and the Effect of Differential Diffusion

Suo Yang *, Xingjian Wang**, Wenting Sun, and Vigor Yang

School of Aerospace Engineering, Georgia Institute of Technology, Atlanta, GA, USA

ABSTRACT

In this study, large eddy simulations (LES) are conducted using both a finite-rate chemistry (FRC) model and a flamelet/progress-variable (FPV) model for a series of piloted partially premixed methane/air flames of increasing turbulence intensity (Sandia Flames D, E, and F). From Flame D to E to F, as flow velocity and strain rate increase, the flame is either pushed downstream and extended radially or weakened by enhanced local extinction. The two combustion models produce different spatial distributions of both time-averaged quantities and instantaneous flame field. The FPV model provides an overall better prediction of the time-averaged axial and radial profiles of Flame D, but a significantly worse prediction of Flame F, primarily because the FPV model significantly over predicts local extinction. In terms of the conditional statistics, in which the effects of spatial distribution of mixture fraction and subgrid-scale (SGS) modeling are largely "removed," the FRC model provides better predictions than the FPV model for all quantities at most locations and mixture fractions in all three flames. The effect of differential diffusion on the prediction of a species depends on the molecular diffusivity of that species; the effect is typically smaller than the difference between the FRC and FPV models.

ARTICLE HISTORY
Received 12 October 2019
Revised 7 April 2020
Accepted 8 April 2020

KEYWORDS
Turbulent combustion; large eddy simulation; finite-rate chemistry; flamelet/progress-variable; differential diffusion

Introduction

Because of the rising demand for combustion energy and its severe environmental impacts, high-fidelity simulation of turbulent combustion has become increasingly important. Over the past three decades, large eddy simulation (LES) has drawn significant attention, and its prediction capability has progressively improved. Numerous LES turbulent combustion models have been developed, and they can be classified into two major categories: finite rate chemistry (FRC) models and reduced-order manifold models. Examples of FRC models are the laminar chemistry model (Gonzalez et al. 2017; Potturi and Edwards 2013), the perfectly-stirred reactor (PSR) model (Lysenko, Ertesvåg, Rian 2014), the partially-stirred reactor (PaSR) model (Marzouk and Huckaby 2010), the linear-eddy model (LEM) (Menon and Kerstein 2011), the Monte Carlo method for Lagrangian filtered probability density function (FDF) transport equations (Pope 1985), and the

CONTACT Vigor Yang vigor.yang@aerospace.gatech.edu School of Aerospace Engineering, Georgia Institute of Technology, Atlanta, GA 30332.

*Current Affiliation: Department of Mechanical Engineering, University of Minnesota – Twin Cities, Minneapolis, MN 55455, USA
**Current Affiliation: Department of Mechanical and Civil Engineering, Florida Institute of Technology, Melbourne, Florida 32901, USA

thickened flame model (TFM) (Legier, Poinsot, Veynante 2000). Examples of the reduced-order manifold models are the steady laminar flamelet model (Peters 1984), the Lagrangian flamelet model (Pitsch and Steiner 2000a, 2000b), and the flamelet/progress-variable (FPV) model (Pierce and Moin 2004).

An advanced reduced-order manifold model, the FPV model (Huo and Yang 2017; Pierce and Moin 2004; Yang, Lew, Mueller 2019a) was developed to account for a low level of local extinction, re-ignition, and unsteady mixing (Pierce and Moin 2004). It incorporates a transport equation to track a progress variable, but it cannot handle multiple-feed streams without a third parameter or more. Using three or more parameters makes the look-up library very difficult to handle, due to the excessive computer memory requirements and the enormous time required to build up the library. Furthermore, a higher-dimensional look-up library requires more efficient data retrieval processes, and a coarser table grid often introduces larger interpolation errors.

To overcome the above limitations, detailed FRC models are preferred. Previous studies have shown that the accuracy of the simple laminar chemistry model is similar to that of other classical Eulerian subgrid-scale (SGS) closure models (Gonzalez et al. 2017; Potturi and Edwards 2013), so the laminar chemistry model is used in the present study. Compared to reduced-order manifold models, detailed FRC models are computationally intensive for LES application because of the large number of species transport equations and their associated numerical stiffness. To reduce computational requirements, conventional FRC-LES often uses over-simplified chemical kinetic models, but this induces significant deviations, especially for low temperature chemistry (Ju et al. 2016; Rousso et al. 2017; Zhang et al. 2017, Chen et al. 2019). To tackle this challenge, a regime-independent framework of a point-implicit stiff ODE solver (ODEPIM) (Bussing and Murman 1988; Katta and Roquemore 2008) and a correlated dynamic adaptive chemistry package (CoDAC) (Sun et al. 2015) were developed. CoDAC generates locally reduced chemical models for different spatial locations and time steps, and only calculates the reaction rates of selected species and reactions. This framework (Yang 2017) has been comprehensively evaluated in simulations of laminar plasma-assisted combustion (Yang et al. 2016a, 2017a, 2015, 2016b), and in direct numerical simulations (DNS) of turbulent premixed (Yang et al. 2017b) and non-premixed (Yang et al. 2017c) flames. The framework accelerates the chemistry solver significantly (20–50 times), and this allows FRC LES using chemical kinetic models of reasonable size in a computationally efficient manner.

In our previous study (Yang et al. 2019b), for the first time, this efficient framework for FRC was incorporated into a preconditioning scheme (Hsieh and Yang 1997; Meng and Yang 2003; Zong and Yang 2007) to enable an Eulerian LES in a fully compressible computational fluid dynamics (CFD) solver, whose range of applicability is much broader than low Mach solvers. This framework was applied to a low Mach number piloted turbulent partially premixed flame (Sandia Flame D). In the present study, the same framework is used to investigate Flames E and F, which have higher bulk velocity and shear strain rate (thus turbulent intensity) than Flame D, and therefore more local extinction and unstable events. Specifically, the Reynolds numbers of Flames D, E, and F are 22400, 33600, and 44800, respectively. The results for Flames E and F are compared to those of Flame D from the previous study using the same model.

Compared to Flame D, there have been significantly fewer studies of Flames E and F, and most of them have employed low Mach number CFD solvers. The FPV reduced-order

manifold model has been employed for Flames D and E (Ihme and Pitsch 2008). Among the FRC models, most of the reported studies employed transported FDF models, including both Lagrangian (Flame D and E) (Raman and Pitsch 2007) and Eulerian (Flames D-F) (Jones and Prasad 2010) FDF models.

To the best of our knowledge, direct comparisons between reduced-order manifold and FRC models have never been made for Flames E and F. Here, therefore, the results from the laminar chemistry FRC model are systematically compared to results from both the FPV model and the experimental data for all Sandia flames. For self-consistency, both combustion models are coupled with a fully compressible CFD solver using a preconditioning scheme (Hsieh and Yang 1997; Meng and Yang 2003; Zong and Yang 2007), whose range of applicability is much broader than low Mach number solvers. In addition, the effect of differential diffusion is evaluated to differentiate it from the effect of chemistry modeling.

Theoretical formulation

The Favre-averaged fully compressible Navier-Stokes equations of mass, momentum, and energy are presented as follows:

$$\frac{\partial \bar{\rho}}{\partial t} + \frac{\partial \bar{\rho}\tilde{u}_i}{\partial x_i} = 0 \tag{1}$$

$$\frac{\partial \bar{\rho}\tilde{u}_i}{\partial t} + \frac{\partial\left(\bar{\rho}\tilde{u}_i\tilde{u}_j + \bar{p}\delta_{ij}\right)}{\partial x_j} = \frac{\partial\left(\tilde{\tau}_{ij} - \tau_{ij}^{sgs}\right)}{\partial x_j} \tag{2}$$

$$\frac{\partial \bar{\rho}\tilde{E}}{\partial t} + \frac{\partial\left(\left(\bar{\rho}\tilde{E} + \bar{p}\right)\tilde{u}_i\right)}{\partial x_i} = \frac{\partial}{\partial x_i}\left(\bar{q}_i + \tilde{u}_j\tilde{\tau}_{ij} - Q_i^{sgs} - H_i^{sgs} + \sigma_i^{sgs}\right) \tag{3}$$

In Eq. (2), the pressure gradient term $\frac{\partial \bar{p}\delta_{ij}}{\partial x_j}$ is proportional to $1/M^2$. In low Mach number flows, this term becomes singular and introduces large numerical challenges, and this requires an extremely small time step and makes the simulation computationally infeasible. A viable solution is to employ a preconditioning scheme (Hsieh and Yang 1997; Meng and Yang 2003; Zong and Yang 2007) for a fully compressible solver, whose range of applicability is much broader than low Mach number solvers. The unclosed terms in Eqs. (1–4) are the SGS terms, which are closed by algebraic Smagorinsky type models (Moin et al. 1991; Smagorinsky 1963; Unnikrishnan et al. 2017).

In this study, two combustion models are considered: an FPV model and an FRC model. The following sections describe in detail the formulation of both models.

Finite-Rate Chemistry (FRC) model

FRC models are preferred to handle flows that involve variable molecular Lewis numbers for differential diffusion, extinction, ignition, emissions, and multi-mode combustion. In this study, the detailed species transport equations are tracked in an Eulerian formulation. The Favre-averaged fully compressible equation of the k-th species is presented as follows:

$$\frac{\partial \bar{\rho}\tilde{Y}_k}{\partial t}+\frac{\partial\left(\bar{\rho}\tilde{u}_j\tilde{Y}_k\right)}{\partial x_j}=\frac{\partial}{\partial x_j}\left(\bar{\rho}\tilde{U}_{k,j}\tilde{Y}_k-\Phi_{k,j}^{sgs}\right)+\bar{\dot{\omega}}_k=\frac{\partial}{\partial x_j}\left(\bar{\rho}D_{k,eff}\frac{\partial \tilde{Y}_k}{\partial x_j}\right)+\bar{\dot{\omega}}_k \tag{4}$$

where the effective diffusivity of the k-th species $D_{k,eff}=D_k+D_{k,t}=D_k+\frac{\mu_t}{\bar{\rho}Pr_tLe_t}$, D_k is the molecular diffusivity of the k-th species, $D_{k,t}$ is the SGS turbulent diffusivity of the k-th species, and μ_t is the SGS turbulent viscosity calculated from the algebraic Smagorinsky-type model. SGS turbulent Prandtl number $Pr_t=0.7$ and SGS turbulent Lewis number $Le_t=1$ are used in this study. The unclosed term $\bar{\dot{\omega}}_k$ on the right-hand side in Eq. (4) is the filtered species net mass production rate. For simplicity, $\bar{\dot{\omega}}_k$ is modeled by the laminar chemistry model, because past investigations have shown that its accuracy is similar to that of other, more complex, classical Eulerian SGS closure models (Gonzalez et al. 2017; Potturi and Edwards 2013). The chemical source terms introduce a large and stiff ODE system, rendering the detailed FRC model computationally prohibitive. In the implementation, the ODEPIM (Bussing and Murman 1988; Katta and Roquemore 2008) and CoDAC (Sun et al. 2015; Yang et al. 2017b, 2017c, 2016b) techniques are utilized to accelerate the calculation.

Flamelet/Progress Variable (FPV) model

In the FPV model (Huo and Yang 2017; Pierce and Moin 2004), instead of solving the transport equations of filtered chemical species, we solve the transport equations of the filtered mixture fraction and progress variable:

$$\frac{\partial \bar{\rho}\tilde{Z}}{\partial t}+\frac{\partial\left(\bar{\rho}\tilde{u}_i\tilde{Z}\right)}{\partial x_i}=\frac{\partial}{\partial x_i}\left(\bar{\rho}D_{eff}\frac{\partial \tilde{Z}}{\partial x_i}\right) \tag{5}$$

$$\frac{\partial \bar{\rho}\tilde{C}}{\partial t}+\frac{\partial\left(\bar{\rho}\tilde{u}_i\tilde{C}\right)}{\partial x_i}=\frac{\partial}{\partial x_i}\left(\bar{\rho}D_{eff}\frac{\partial \tilde{C}}{\partial x_i}\right)+\bar{\dot{\omega}}_C \tag{6}$$

Without solving the transport equations of filtered chemical species, the FPV model assumes a unity Lewis number for the effective diffusivity D_{eff} $\left(\text{i.e., } D_{eff}=\frac{\lambda_{eff}}{\bar{\rho}\tilde{c}_p}\right)$, and the effective thermal conductivity $\lambda_{eff}=\lambda+\frac{\tilde{c}_p\mu_t}{Pr_t}$, where λ is the molecular thermal conductivity. $Pr_t=0.7$ is used in this study. The model therefore cannot directly capture the differential diffusion effects, although it can partially capture the effects by tabulation using flamelet solutions with differential diffusion. In regions with low turbulence intensity, turbulent diffusivity becomes negligible, and differential molecular diffusion effects could be important, leading to relatively substantial errors of the FPV model. On the other hand, in regions with high turbulence intensity, turbulent diffusion can be very important and even dominant, so that the effective differential diffusion approach used in the FRC model is not necessarily better than the unity effective Lewis number approach in the FPV model to represent the transport process.

In the present study, the Bilger mixture fraction Z (Bilger 1993) is defined as:

$$Z = \frac{0.5 \times \frac{Y_H - Y_{H,coflow}}{W_H} + 2 \times \frac{Y_C - Y_{C,coflow}}{W_C}}{0.5 \times \frac{Y_{H,jet} - Y_{H,coflow}}{W_H} + 2 \times \frac{Y_{C,jet} - Y_{C,coflow}}{W_C}} \tag{7}$$

where the 'coflow' subscript represents the co-flow feed, the 'jet' subscript represents the main fuel jet feed, and the other quantities are the measured samples. The progress variable C is simply defined as:

$$C = Y_{CO} + Y_{CO_2} + Y_{H_2} + Y_{H_2O} \tag{8}$$

During the simulation, the filtered species mass fractions are retrieved from the library as functions of filtered mixture fraction, its variance, and the filtered progress variable. This could cover part of the unstable branch of the S-shaped curve of ignition and extinction, and hence could partially account for the unsteady effects.

Results and discussion

The Sandia flames (Barlow and Frank 1998) have been fully characterized through a series of detailed experiments on a piloted turbulent partially premixed methane/air flame configuration. From Flame D to Flame F, the bulk velocities of both fuel jet and piloted flame are increased (see Table 1). Full experimental data sets are available, and the flames have been simulated many times for validation purposes (Jones and Prasad 2010; Pitsch and Steiner 2000a; Raman and Pitsch 2007). In this study, Flames D, E, and F are simulated using both the FRC and FPV models. To the best of our knowledge, this work is the first attempt to employ a fully compressible solver with an Eulerian FRC model for Flames E and F. The detailed flow conditions are presented in Table 1. Unlike previous studies using low Mach number CFD solvers, the present work employs a fully compressible CFD solver with a preconditioning scheme, whose range of applicability is much broader than those of low Mach number solvers.

The computational domain is from 6 mm upstream of the inlet to 600 mm downstream of the inlet, 36 mm in the radial direction at inlet, and 150 mm in the radial direction at the end of the domain. We use 310 grid points in the axial direction, 130 points in the radial direction, and 64 points in the azimuthal direction. Grid clustering is employed to resolve the high gradient regions near both the inner and outer shear layers. The total number of grid points is approximately 2.6 million. The experimentally specified velocity profile and turbulence intensity are enforced at the inlet, while a fixed back pressure is set

Table 1. Flow conditions of Sandia Flames D, E, and F (Barlow and Frank 1998).

	Composition	Inner diameter (mm)	Outer diameter (mm)	Bulk velocity (m/s)	Temperature (K)
Fuel jet	25% CH_4/75% air (by volume)	7.2	7.7	D: 49.6 E: 74.4 F: 99.2	294
Piloted flame	Equilibrium: CH_4/air mixture ($\phi = 0.77$)	7.7	18.2	D: 11.4 E: 17.1 F: 22.8	1880
Coflow	Air	18.9	N/A	0.9	291

at the outlet. A methane chemical mechanism with 20 species and 84 reactions (Yang et al. 2019b) is used in both combustion models. The chemical mechanism was reduced from GRI-Mech 3.0 (Smith et al.) using the Global Pathway Selection (GPS) algorithm (Gao, Yang, Sun 2016) and verified in terms of homogeneous ignition delays, extinction curves in the perfectly-stirred reactor (PSR), and laminar flame speeds. The time-averaged statistics are calculated after three flow-through-times, to allow the flow field to reach its statistically stationary state.

Spatial distribution of reactivity

Figure 1 shows instantaneous spatial distributions of numbers of active species and reactions for the three flames, generated from the CoDAC method (threshold = 2%). CoDAC generates locally reduced chemical kinetics for each spatial location and time step, and each locally reduced chemical mechanism has small numbers of active/remaining species and reactions (often much smaller than the full mechanism) to represent the reactivity of the location and time step. These numbers are good indicators for the level of reactivity. In the zone outside the expanding jet brush, only 2 species (preselected seed species: fuel and oxidizer) and zero reactions are selected, because no chemical reactions occur there. In the highly distributed turbulent partially premixed flame zone, most of the species and reactions in the full mechanism are selected. Note that from Flame D to E to F, due to increased velocity and enhanced mixing, the flame zone is enlarged radially and extended further downstream. There is a large buffer zone (green) between the zone outside the expanding jet brush and the highly distributed turbulent partially premixed

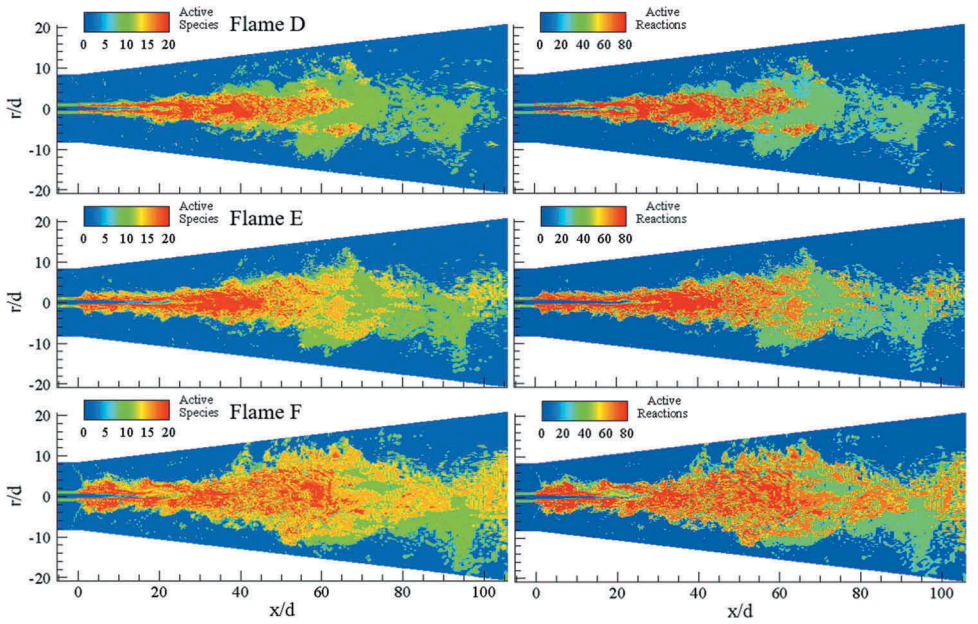

Figure 1. Instantaneous spatial distributions of numbers of active species (left) and reactions (right), generated from the CoDAC method with the FRC-LES approach for Flames D (upper), E (middle), and F (lower).

flame zone, with intermediate numbers of selected species and reactions. Similar to the flame zone with almost full mechanism, from Flame D to E to F, this buffer zone is also enlarged radially and extended axially downstream. The reduction in numbers of species and reactions at most spatial locations is responsible for the acceleration of the chemistry calculation using the CoDAC method.

Figure 2 shows the time-averaged spatial distributions of temperature, calculated by both FRC and FPV approaches. Intense combustion regions can be observed in two of the three flames and in Flame F as predicted by FRC at approximately x/d = 40, where almost complete mixing and combustion are achieved to reach peak temperatures. Flame F as predicted by FPV is almost completely extinguished at that location. Because of the increasingly high bulk velocity in Flames E and F, the flame is either pushed further downstream (from E to F, predicted by FRC) or weakened due to the enhanced local extinction (from D to E to F, predicted by FPV). Overall, the time-averaged spatial distributions predicted by the two approaches are different, and the difference is between the two approaches increases significantly from Flame D to E to F.

Unlike the time-averaged temperature distributions, the instantaneous temperature distributions of the two models are quite different, as shown in Figure 3. The flames all have very dynamic jet flow and flame structures, and some level of local extinction. Near the inlet, the piloted flame shows enhanced combustion stability and minimized local extinction. In the downstream locations, the co-flow and fuel jet interact with each other in the high temperature shear layer, which results in more local extinction. The topological differences between the two models are more apparent than in the time-averaged counterpart.

For Flame E, FRC-LES predicts no flame near the axial center line from the inlet to x/d = 60, but FPV predicts intense combustion regions across the center line, which is consistent with the time-averaged distributions shown in Figure 2. Near the inlet, FRC-LES predicts that the piloted flame can survive further downstream, to wrap around the shear-layer-generated vortices, but the FPV-LES predicts that the piloted flame is quenched much further upstream, before reaching the vortices, which agrees with previous FPV studies (Ihme and Pitsch 2008). This can be explained by low turbulence intensity near the inlet, where the flow field is close to laminar. This fact

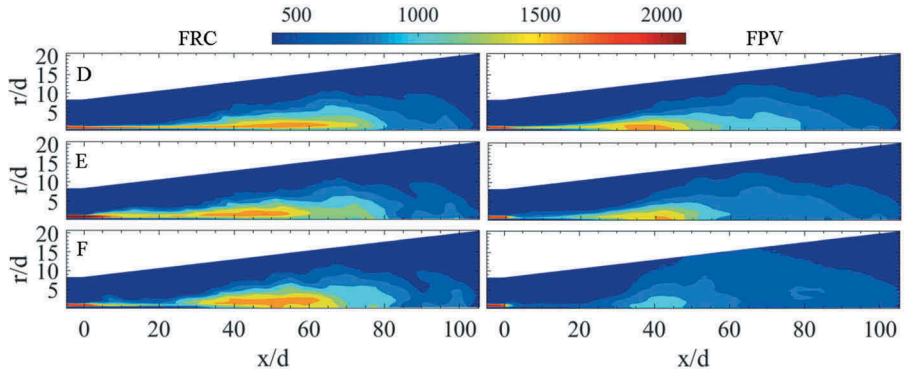

Figure 2. Time-averaged temperature distributions for Flames D (upper), E (middle), and F (lower), using FRC-LES (left) and FPV-LES (right).

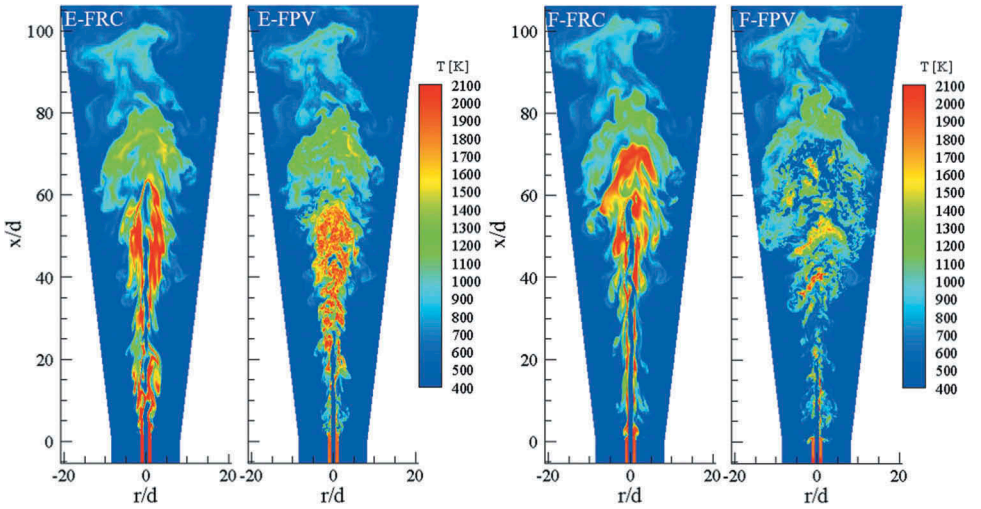

Figure 3. Instantaneous temperature distribution. From left to right: Flame E from FRC-LES and from FPV-LES at the same time instance, Flame F from FRC-LES and from FPV-LES at the same time instance.

indicates that near the inlet (Han, Raman, Chen 2016; Pitsch and Steiner 2000a) the effect of differential molecular diffusion is important, but it cannot be tracked by the FPV model if the unity Lewis number is assumed.

For Flame F, FRC-LES predicts that the flame is pushed further downstream because the bulk velocity is higher than in Flame E, but FPV predicts more significant local extinction and finer structures in the same downstream region, which agrees with the time-averaged distribution in Figure 2. This means that the local scalar dissipation rates in that region are sufficiently high to go beyond the extinction point on the S-curve, but the FRC-LES prediction can deviate from the S-curve to obtain lower local scalar dissipation rates (supported by the data but not shown here), such that the flame is still not extinguished.

In the downstream locations of both Flames E and F, the FPV model predicts relatively smaller high temperature regions than the FRC model, and a completely different topology (more local extinction and finer structures). Unlike for Flame D (Yang et al. 2019b), there are large deviations between the two models in both the upstream and downstream regions. It is not obvious which model is closer to the experiment, because a quantitative experimental measurement of instantaneous temperature distribution is not available. Considering the relevance to unsteady/un-stationary phenomena such as ignition, extinction/lean blow-out (Esclapez et al. 2017), and combustion instability (Li et al. 2017), the above differences between the two models are important issues.

To better understand these differences, detailed spatial distributions of species are presented. Figure 4 compares the instantaneous distributions of OH radical predicted by the two models for Flames E and F. The OH profiles from both models are extended further downstream in Flame F due to the higher bulk velocity. For Flame E, in the upstream locations ($x/d < 20$), the FRC model predicts significantly higher OH concentration than in its FPV counterpart, and this agrees with the early quenching of the piloted flame predicted by the FPV model in Figure 3. In the downstream locations, the FPV

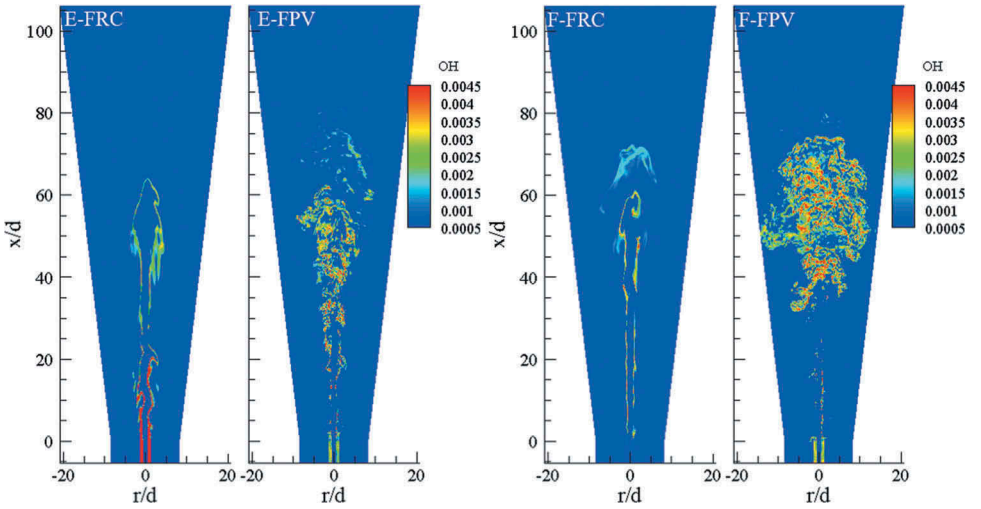

Figure 4. Instantaneous Y_{OH} distribution for Flames E and F with different combustion models.

model predicts much broader regions with high OH concentration for both flames. In the same locations, however, the FPV model predicts smaller high temperature regions and more local extinction, especially for Flame F, as shown in Figure 3. This seems to contradict the general understanding that higher radical levels indicate stronger heat release and higher temperature.

To explain the aforementioned observation, the instantaneous distributions of CO mass fraction from the two models are compared in Figure 5. As for OH concentration (Figure 4), the CO profiles from both models are extended further downstream in Flame F than in Flame E, due to the increasing bulk velocity. For Flame E, the FPV model

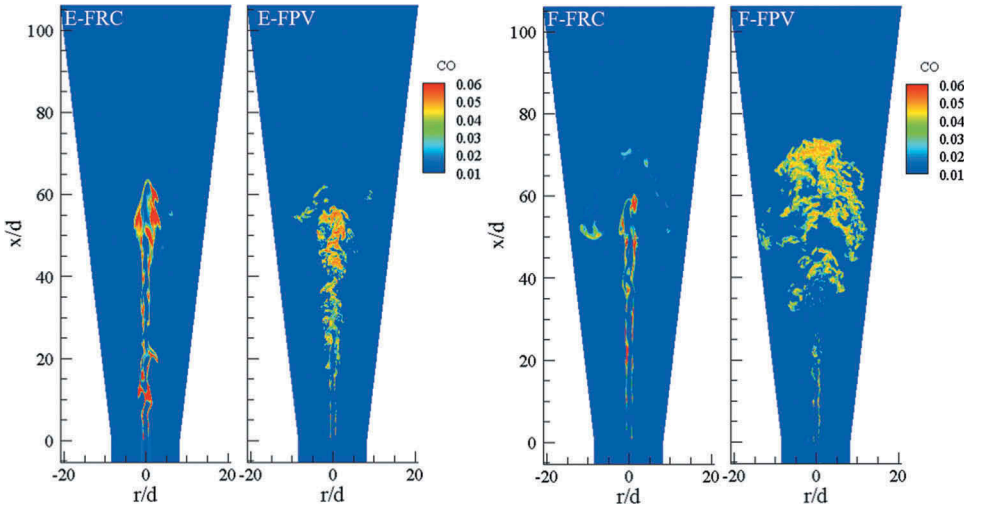

Figure 5. Instantaneous Y_{CO} distribution. From left to right: Flame E from FRC-LES and from FPV-LES at the same time instance, Flame F from FRC-LES from FPV-LES at the same time instance.

predicts lower CO concentration than its FRC counterpart throughout the flow field. Because CO+OH = CO_2 + H is a key heat release reaction and a rate-controlling step, the FPV model predicts significantly smaller high temperature regions (more local extinction and finer structures) and this also partially explains its over-prediction of OH in the downstream locations. The FPV model also predicts a lower concentration of combustion products (CO_2 and H_2O) in the downstream region (not shown here, for brevity), which further confirms the above conclusion. In contrast, for Flame F, although the FRC model still predicts higher peak CO concentration than its FPV counterpart in the downstream locations, the FPV model predicts a broader but broken region of intermediate CO concentration. Considering the intense local extinction shown in Figure 3, for the Flame F predicted by FPV-LES, it is apparent that the strong strain rate first distributes the flame, then extinguishes it locally to create finer structures, but the CO concentration takes a much longer time to decay due to the lack of consumption.

On the other hand, the FPV model predicts smaller regions of high CH_4 concentration for both flames (Figure 6). For this reason, a good portion of the carbon must be carried by intermediate species between CH_4 and CO, primarily CH_2O and HCO (Zhao et al. 2017). The conversion from HCO to CO is rapid, and thus only a very low HCO concentration can be accumulated (up to 10^{-5} by mass fraction). In the database of the FPV table consisting of one-dimensional steady counterflow flamelet solutions, the flame temperature is higher than that under real unsteady conditions in turbulent combustion, so CH_2O+OH = HCO+H_2O tends to dominate the conversion from CH_2O to HCO. In contrast, in Figure 3, many lower temperature (approximately 1200 K) 'holes' are visible in the intense combustion regions; in these regions, CH_2O+O_2 = HCO+HO_2 should dominate the conversion from CH_2O to HCO during the unsteady evolution. However, the steady FPV table cannot capture the unsteady evolution history of the flame and may

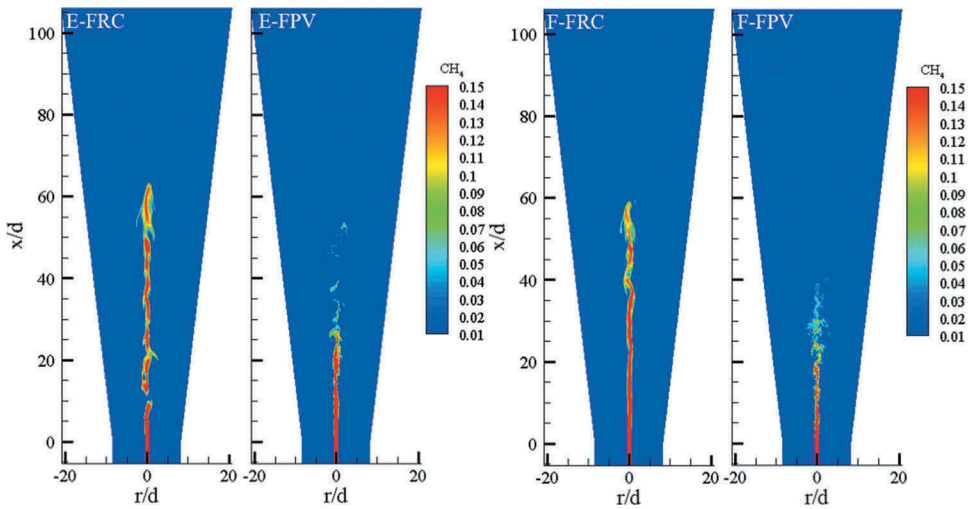

Figure 6. Instantaneous Y_{CH_4} distribution. From left to right: Flame E from FRC-LES and from FPV-LES at the same time instance, Flame F from FRC-LES and from FPV-LES at the same time instance.

overlook this important reaction. Therefore, in those holes, the carbon element in FPV-LES is partially stuck at CH_2O and will tend not to further convert into HCO and CO, as evidenced by CH_2O mass fraction accumulated up to the 10^{-3} level.

The discrepancies between the two models could come from the different transport models (by default: differential diffusion model for FRC-LES and unity Lewis number model for FPV-LES), the FPV library, the unsteady evolution of filtered mixture fraction and progress variable in the FPV model, or some combination of these factors. For this reason, in the following sections, predictions from the two models will be compared with the experimental data, based on: (1) time-averaged axial and radial distributions of temperature and mixture fraction; and (2) time-averaged conditional statistics in the mixture fraction space.

In addition, the effective Lewis numbers of species will approach unity under high turbulence intensity (Wang 2016), because the dominance of turbulent diffusivity over molecular diffusivity is strong. On the other hand, since the state of the art of SGS modeling contains significant uncertainties (typically 100% or larger), SGS turbulent diffusivity $D_{k,t}$ cannot be modeled very well in the FRC model ($D_{k,t} = \frac{\mu_t}{\bar{\rho} Pr_t Le_t}$ in this study). For this reason, FRC-LES using the unity effective Lewis number assumption $\left(\text{i.e., } D_{k,eff} = D_{eff} = \frac{\lambda_{eff}}{\tilde{\rho}\tilde{c}_p} \text{ with } \lambda_{eff} = \lambda + \frac{\tilde{c}_p \mu_t}{Pr_t}\right)$ is also conducted to evaluate the effect of transport model choice for all three flames, such that FRC and FPV use the same transport model. This should make clear whether, and if so how much of, the discrepancy between the results from FRC and FPV is due to differential diffusion.

Axial profiles

Figure 7 shows the axial distributions of the time-averaged statistics for temperature and mixture fraction. The mixture fraction profile becomes steeper from Flame D to E to F due to the enhanced turbulence intensity, but the temperature profile is not pushed downstream significantly. In addition, the peak temperatures are not at the stoichiometric mixture fraction of 0.35 for all three flames. This means that the thermochemical states deviate from the steady flamelet solutions due to the strong local dissipation rates. Both models under-predict the peak values in the intense combustion region (x/d = 40 ~ 60), but the FRV model predicts more accurate peak temperatures than the FRC models do for Flames D and E (which are closer to the "flamelet" regime), and the FRC models predict a more accurate peak temperature than the FPV model for Flame F (which has higher Mach number). The profile of the FRC model with unity Lewis number, even though it is a hybrid of the two default models, is not always located between their profiles. For temperature, the FPV model provides a better prediction at the upstream locations (x/d < 40), in terms of both qualitative trends and quantitative values, while the FRC model is better at the downstream locations (x/d > 50). For mixture fraction, the FPV model provides a better prediction at most locations for Flame D (which is closer to the "flamelet" regime). For Flame F (which has higher Mach number), the FRC models are significantly closer to the experimental data than the FPV model, which erroneously predicts an overly rapid decay of mixture fraction and complete extinction. The profile of the FRC model with unity Lewis number is close to the default FRC model for Flames E and F, but is too high for Flame D.

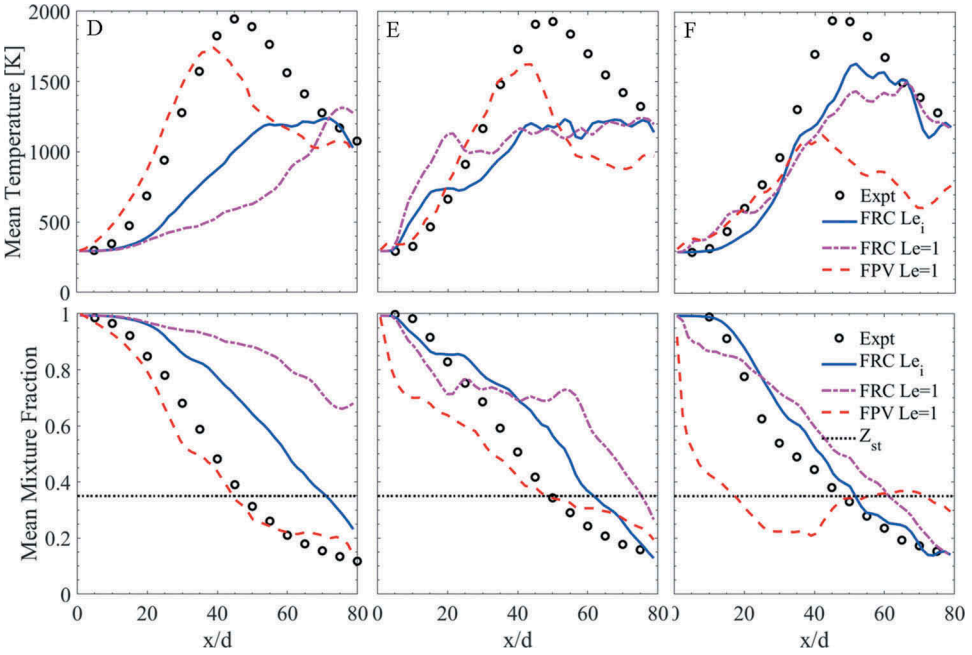

Figure 7. Axial profiles of mean temperature (upper) and mixture fraction (lower) of Flames D (left), E (middle), and F (right), from the experiment, the FRC-LES approach, and the FPV-LES approach. Z_{st} is the stoichiometric mixture fraction of 0.35, Le_i means the differential diffusion model, Le = 1 means the unity Lewis number model.

Radial profiles

Figure 8 shows the radial distributions of time-averaged temperature at four axial locations. At most axial locations, the peak temperature gradually decreases from Flame D to E to F due to the increasing strain rate, except at x/d = 45, which is in the intense combustion region for all three flames. At the upstream locations (x/d = 7.5 and 15) both models agree well with the experiment near the centerline, but mismatch the outer region (r/d > 0.6), especially for Flames E and F. On the contrary, at the downstream locations (x/d = 30 and 45) both models agree with the experimental data in the outer region (except for the FPV model for Flame F) but under-predict near the centerline (except for the FPV model for Flame D at x/d = 30). As in the axial distribution, the FPV model provides slightly better prediction than the FRC models for Flame D, but significantly worse predictions for Flame F. For most locations in the three flames, the FRC-LES with two transport models provide very similar predictions.

Figure 9 shows the radial distributions of time-averaged mixture fraction at different axial locations. The time-averaged mixture fraction near the centerline gradually decreases along the axial direction, indicating significant entrainment/mixing of the fuel jet with pilot and coflow. Predictions from both FRC and FPV models are in fairly good agreement with experimental data (except FPV model for Flame F), and are significantly better than the temperature predictions. Near the centerline, the FRC models often over-predict the mean mixture fraction, possibly due to their over-prediction of fuel jet entrainment and mixing in that region. In contrast, the FPV model always under-predicts the centerline mixture fraction. As noted with respect to temperature, the FPV model provides a better

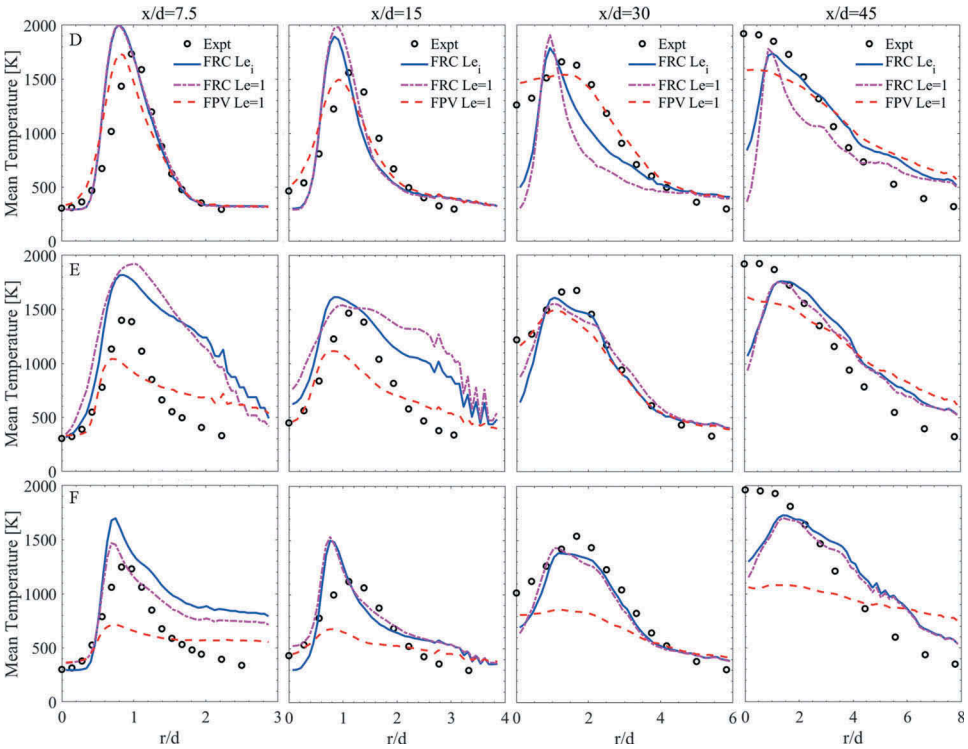

Figure 8. Radial profiles of time-averaged temperature of Flame D (upper), E (middle), and F (lower), from the experiment, the FRC-LES approach, and the FPV-LES approach. Le_i means the differential diffusion model, Le = 1 means the unity Lewis number model.

prediction than the FRC models for Flame D, but a worse prediction for Flame F. Far away from the centerline, the predictions of the two models are relatively closer to each other. The effect of the transport model is relatively small, and the profile of the FRC model with unity Lewis number does not always appear between the profiles of the two default models.

In summary, the FPV model provides slightly better predictions than the FRC models for Flame D, but significantly worse predictions for Flame F. The relatively poor performance of the FPV for Flame F is because the FRC models more accurately capture extinction and ignition. The predictions of FRC-LES using different transport models are often close to each other, which suggests that the effect of transport modeling is relatively small. In addition, the profile of the FRC model with unity Lewis number does not always reside between the profiles of the two default models. Therefore, when the FPV model is slightly better at predicting spatial distribution than the FRC models (e.g., Flame D), it may be because of the lack of SGS modeling of chemical source terms in the FRC model.

Conditional statistics

The FPV model predictions differ from those of the FRC models partly due to their different predictions of the spatial distribution of mixture fraction. To compare other

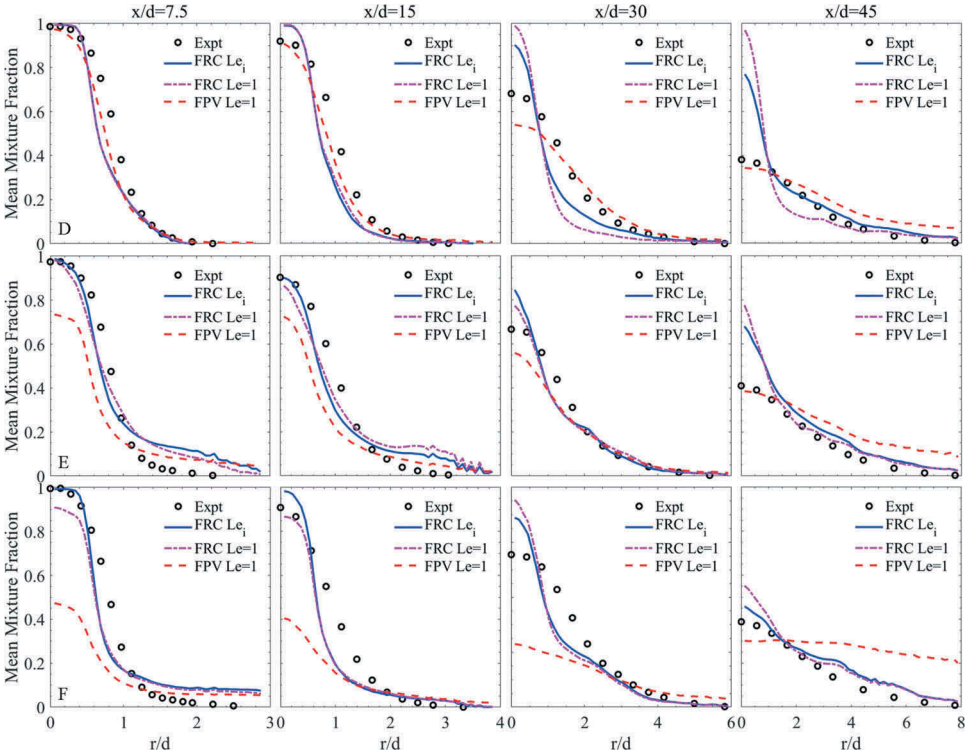

Figure 9. Radial profiles of time-averaged mixture fraction of Flame D (upper), E (middle), and F (lower), from the experiment, FRC-LES approach, and FPV-LES approach. Le_i: differential diffusion model, Le = 1: unity Lewis number model.

aspects of the two models, especially the chemical kinetics, we need to partially "remove" the effects of spatial distribution and SGS modeling by investigating the conditional statistics in the mixture fraction space. Furthermore, the conditional statistics can also offer insight into the turbulence/chemistry interactions and illustrate the difference between the FPV tabulation and FRC.

Figure 10 shows the conditional mean temperature at four axial locations, for which the experimental data contains 3% systematic uncertainty. From Flame D to E to F, for most axial locations (x/d = 7.5, 15, and 30), the peak temperature is decreasing due to the higher strain rate. Results from the FRC models agree better with the experimental data than their FPV counterparts for all locations and flames and almost all mixture fraction values, especially for Flames E and F, due to the over-prediction of extinction from FPV. The predictions of the FRC-LES approach are better in the upstream locations than in the downstream locations. In the downstream locations (x/d = 30 and 45), both models agree well with the experimental data on the fuel lean side, but under-predict the mean temperature on the fuel rich side. The FRC model with unity Lewis number predicts profiles that are similar to those of the FRC model with differential diffusion, which confirms that the effective Lewis numbers of species responsible for heat release are close to unity. Due to the entrainment/mixing of the fuel jet with the pilot and coflow in the downstream locations, all profiles end up with mixture fraction values significantly smaller

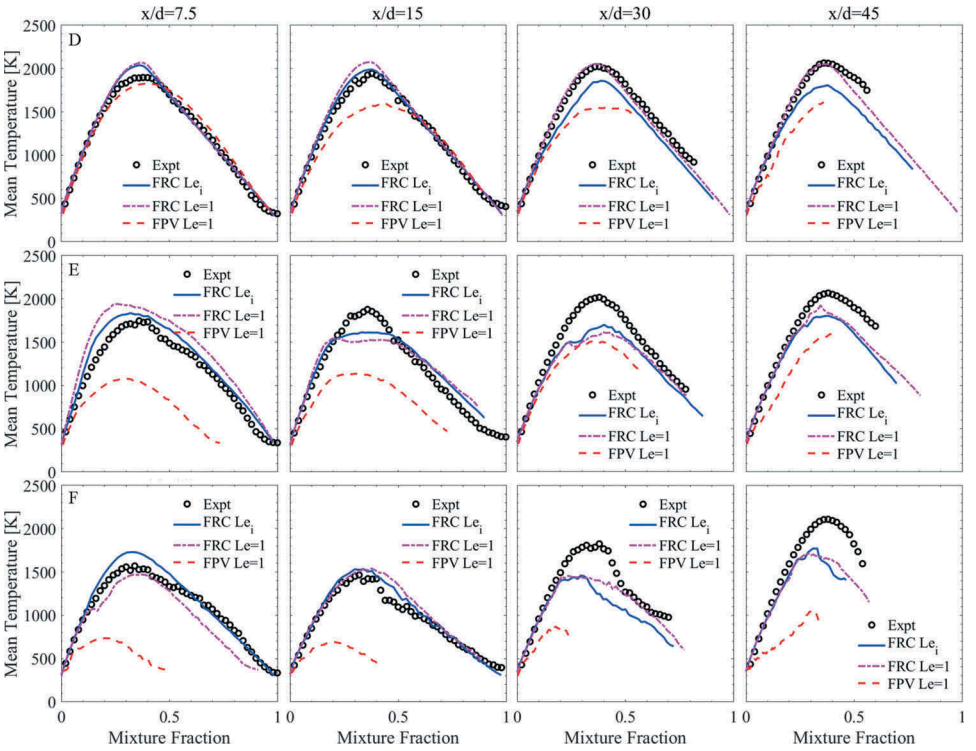

Figure 10. Conditional average of temperature for Flames D (upper), E (middle), and F (lower), from the experiment, FRC-LES approach, and FPV-LES approach. Le_i: differential diffusion model, Le = 1: unity Lewis number model.

than unity. Of course, a given location could be lean, stoichiometric, or rich at different time instances. In that case, the time-averaged data at a single location will include instantaneous lean, stoichiometric, and rich data, and the trends will partially offset each other, such that the mean data will show smaller differences than the instantaneous data (Figures 2 and 3).

Figure 11 shows the conditional mean of Y_{H_2O} to represent major combustion products, for which the experimental data contains 4% systematic uncertainty. The performance of the two models is like their predictions for the time-averaged conditional temperature, which indicates that most of the heat release is closely correlated with the formation of H_2O. From Flame D to E to F, for most axial locations (x/d = 7.5, 15, and 30), the peak Y_{H_2O} value is decreasing due to the higher strain rate. For all three flames, the value of Y_{H_2O} at x/d = 45 is higher than that at x/d = 15, and this is probably attributable to re-ignition. Furthermore, the partially premixed burning (the triple-flame structure) at x/d = 45 creates a plateau region in the Y_{H_2O} profile, which does not exist in pure diffusion flames. Results from the FRC model agree better than the FPV model with the experimental data for all the locations and flames, especially at the upstream locations (x/d = 7.5 and 15). In some upstream locations (x/d = 7.5 and 15 of Flame D and F), the FRC model agrees very well with the experimental data for almost

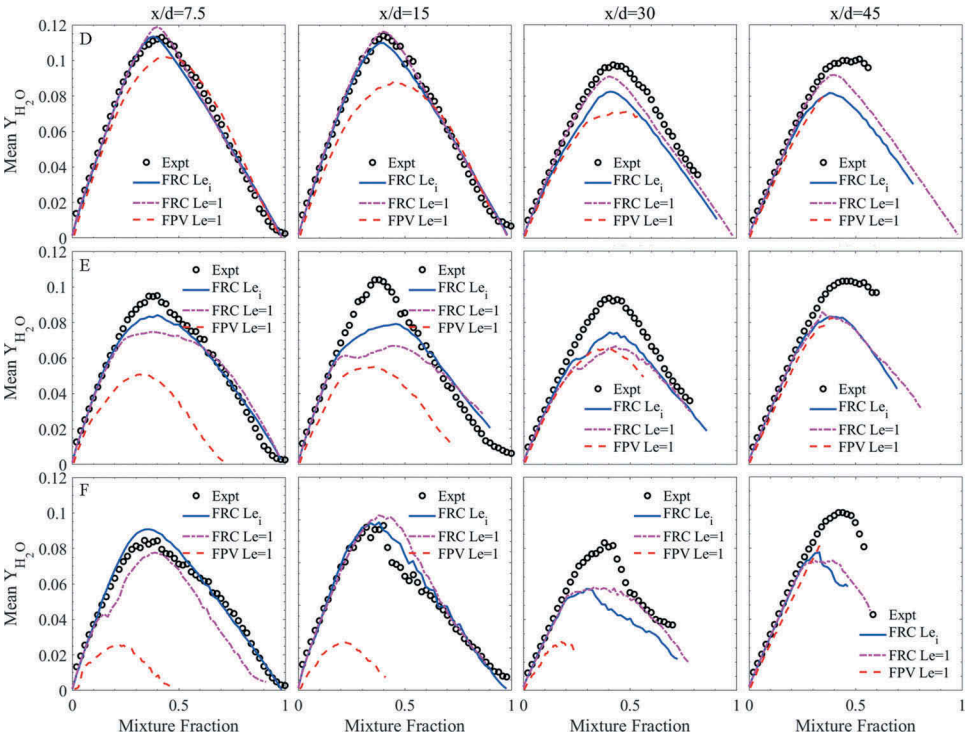

Figure 11. Conditional average of Y_{H_2O} of Flames D (upper), E (middle), and F (lower), from the experiment, FRC-LES approach, and FPV-LES approach. Le$_i$: differential diffusion model, Le = 1: unity Lewis number model.

all mixture fraction values. Like the temperature results, both models can provide good prediction on the fuel-lean side. Near the stoichiometric mixture fraction of $Z = 0.35$ and on the rich side, however, the FPV model predicts significantly smaller H_2O concentration than the FRC model. As in the temperature profiles, for Flame F, the FRC model with unity Lewis number predicts similar profiles as the FRC model with differential diffusion; the differences are slightly larger than for temperature, because the molecular diffusivity of H_2O is approximately 0.8.

Figure 12 shows the conditional mean of Y_{OH}, representing radical species, for which the experimental data contain 10% systematic uncertainty. At upstream locations (x/d = 7.5 and 15), the results from the default FRC model agree with the experimental data very well (except for x/d = 15 of Flame E), while the FPV model predicts significantly lower peak values. From Flames D to E to F, the peak value decreases. At the downstream locations (x/d = 30 and 45), both default models significantly under-predict the peak values for all the flames, and the peak values of the three flames are similar, but the FRC model with unity Lewis number captures the peak values of Flame D very well. On both the lean and rich sides of the flames, the predictions from the FRC models agree better with the experimental data than does the FPV counterpart. The differences between the unity Lewis number and differential diffusion models are greater than in the H_2O profiles, because the molecular diffusivity of OH is approximately 0.7, which is further from unity.

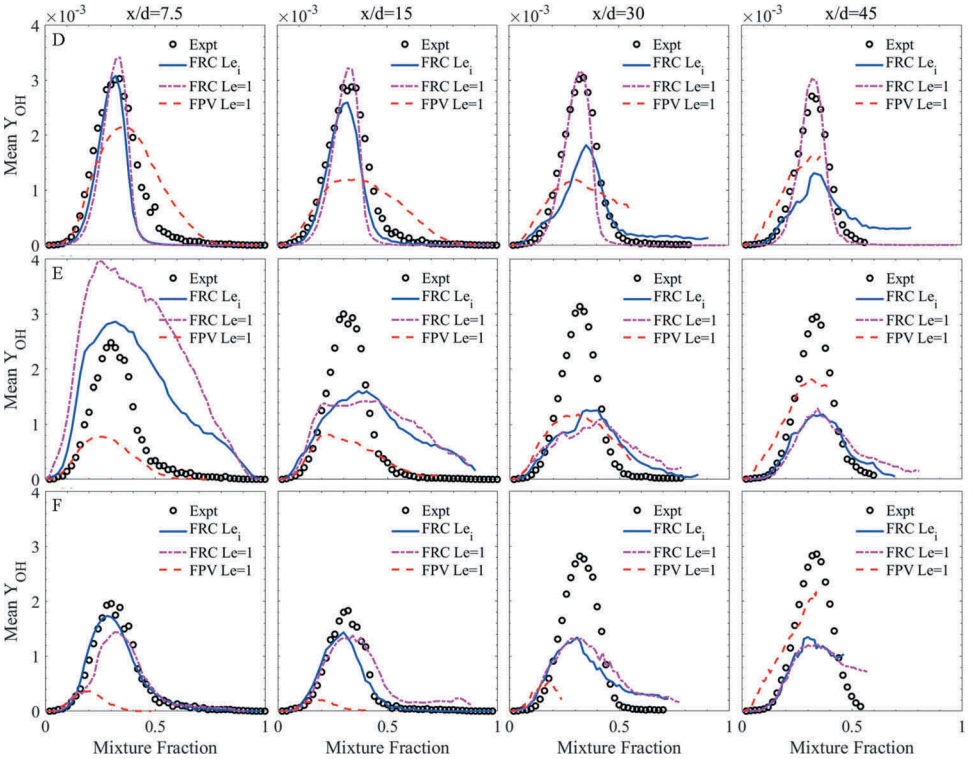

Figure 12. Conditional average of Y_{OH} of Flame D (upper), E (middle), and F (lower), from the experiment, FRC-LES approach, and FPV-LES approach. Le_i: differential diffusion model, Le = 1: unity Lewis number model.

Figure 13 shows the conditional mean of Y_{CO}, representing intermediate species, for which the experiment data have 10% ~ 20% systematic uncertainty. From Flame D to E to F, the peak CO concentration decreases, except at the furthest downstream location of x/d = 45. This observation agrees with similar observations in temperature, H_2O, and OH. For all locations and flames, the very lean and very rich regions contain relatively smaller errors, and both default models under-predict the peak values at the downstream locations (x/d = 30 and 45). This partially explains the under-prediction of peak temperature (seen in Figure 10) in the same locations. But the default FRC model results have peak values significantly closer to the experimental data than their FPV counterparts, especially at the upstream locations (x/d = 7.5 and 15) of Flames D and F.

For the downstream locations (x/d = 30 and 45) of Flame D, the FRC model with unity Lewis number predicts peak values significantly closer to the experimental data than either of the default models. In contrast, some previous FRC (Jones and Prasad 2010) and FPV (Ihme and Pitsch 2008) studies, both of which employed low Mach number solvers, over-predicted the peak values. In particular, one previous FRC study (Jones and Prasad 2010) employed a chemical mechanism (19 species, reduced from GRI-Mech 3.0) similar to the one used in the present study, so the opposite trend in conditional mean of Y_{CO} is probably not due to different chemical mechanisms, but rather to the different choice of

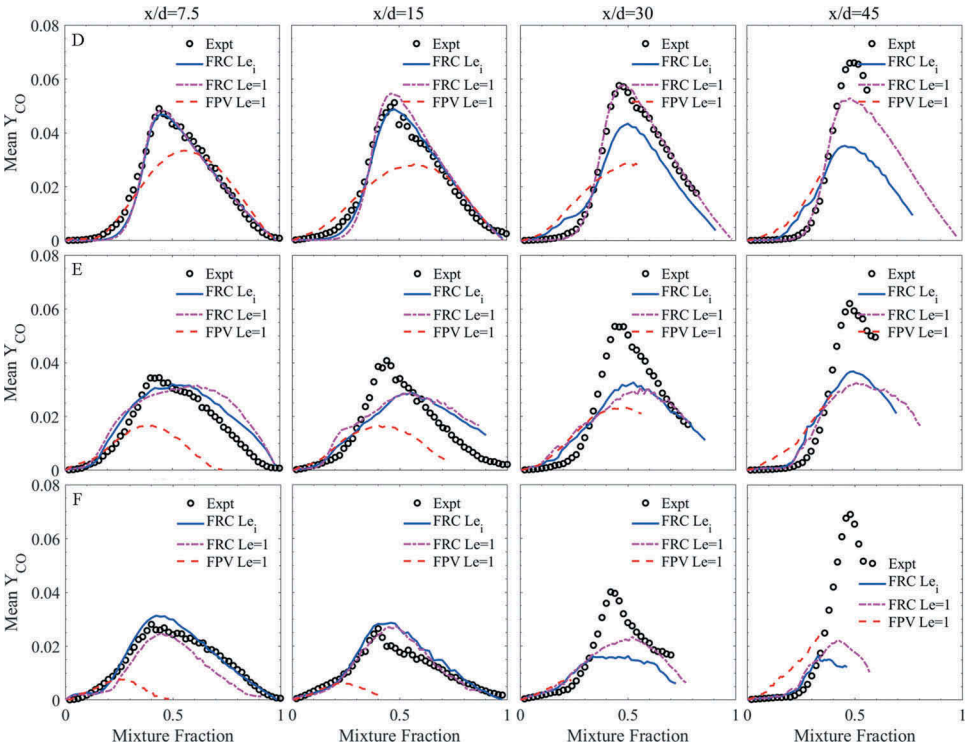

Figure 13. Conditional average of Y_{CO} of Flame D (upper), E (middle), and F (lower), from the experiment, FRC-LES approach, and FPV-LES approach. Le_i: differential diffusion model, Le = 1: unity Lewis number model.

CFD solvers. At the furthest upstream location (x/d = 7.5), the influence of the piloted flame dominates, such that the peak value of Y_{CO} cannot directly represent the peak value of temperature.

The FRC models predict better peak values and lean profiles for temperature, H_2O, and OH than their FPV counterparts at all locations of all flames. Near $Z = 0.5$, the FPV model predicts significantly smaller CO concentration than the FRC model, which is consistent with the limiting effect of CO for the FPV prediction observed in snapshots (Figure 5). On the very fuel-rich side, the CO concentration predicted by the FPV model is always far lower than that from the FRC model.

Figure 14 shows the conditional mean of Y_{CH_4}. All models and the experiment show monotonically increasing profiles, which follows the definition of mixture fraction. No significant difference is observed among the three flames, except that the profiles for Flame F are shorter than for Flames D and E at the downstream locations (x/d = 30 and 45). At most locations (x/d = 7.5, 15, and 30), the predictions from the two FRC models are close to each other and agree well with the experimental data, but the FPV model over-predicts the profiles. At x/d = 45, both models significantly over-predict the Y_{CH_4} level on the fuel rich side. The two FRC transport models predict similar CH_4 profiles, because the molecular diffusivity of CH_4 is also approximately unity.

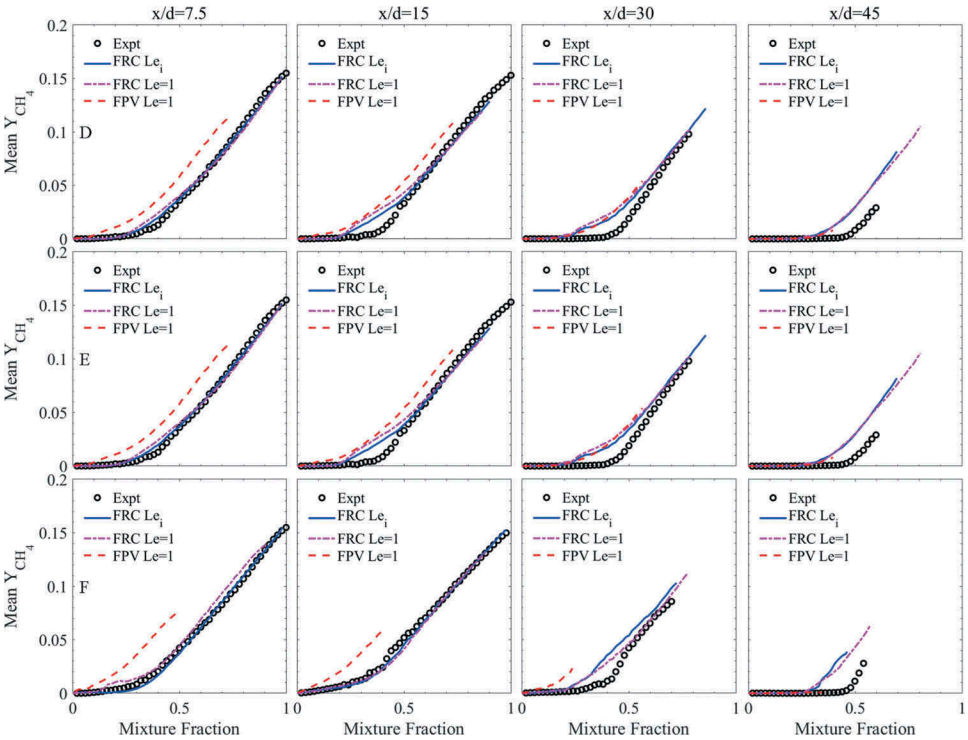

Figure 14. Conditional average of Y_{CH_4} of Flame D (upper), E (middle), and F (lower), from the experiment, FRC-LES approach, and FPV-LES approach. Le_i: differential diffusion model, Le = 1: unity Lewis number model.

Conclusions and recommendations for future work

In this study, large eddy simulations (LES) are conducted using the finite-rate chemistry (FRC) and flamelet/progress-variable (FPV) models for a series of piloted partially premixed methane/air flames with high turbulence intensity and low levels of local extinction and re-ignition, Sandia Flames D, E, and F. From Flame D to E to F, due to the increase in flow velocity and strain rate, the flame zone is either pushed downstream and extended radially or weakened by enhanced local extinction. The two models produce different spatial distributions of both time-averaged quantities and instantaneous flame field. In particular, the FPV model incorrectly predicts intense local extinction for Flame E and complete extinction for Flame F, while the FRC model provides reasonably good agreement with the experimental data. The time-averaged axial and radial profiles of all the three flames show that the FPV model provides an overall better prediction than the FRC model for Flame D, but a significantly worse prediction for Flame F, primarily due to the over-prediction of local extinction by the FPV model. The FRC model with unity Lewis number predicts spatial distributions similar to those of the FRC model with differential diffusion, but its profiles are not always located between those of the two default FRC and FPV models. The effect of differential diffusion is relatively small with respect to the discrepancy between the FRC and FPV models, and the SGS modeling of chemical source term might play a more important role. In the conditional statistics on the three flames, in

which the effects of spatial distribution of mixture fraction and subgrid-scale (SGS) modeling are partially "removed," the FRC models provide better predictions than the FPV model for all quantities at most locations and mixture fractions. In the mixture fraction space, the difference in species concentration predictions between the two transport models depends on how close the molecular diffusivity of a given species is to unity, and neither of the two transport models is always better. The present results suggest that to properly apply FRC in LES, better transport models covering a broad range of turbulence intensity will be required. In such models, the dependence on Reynolds number (Wang 2016) and the strain-sensitivity of chemical species (Lew, Yang, Mueller 2017) should be considered. This topic should be addressed in future work.

Nomenclature

$\tilde{C}$	Favre-filtered progress variable
$\tilde{c}_p$	Favre-filtered heat capacity at constant pressure ($J \cdot kg^{-1} \cdot K^{-1}$)
d	jet diameter (m)
D_k	molecular diffusivity of the k-th species (m^2/s)
$D_{k,eff}$	effective diffusivity of the k-th species (m^2/s)
D_{eff}	effective diffusivity of mixture fraction and progress variable (m^2/s)
$D_{k,t}$	sub-grid scale turbulent diffusivity of the k-th species (m^2/s)
$\tilde{E}$	Favre-filtered total energy ($J \cdot kg^{-1}$)
H_i^{sgs}	sub-grid scale energy flux in the i^{th} direction ($J \cdot m^{-2} \cdot s^{-1}$)
$\tilde{k}_{bi}$	Favre-filtered backward reaction rate constant of the i^{th} reaction
$\tilde{k}_{fi}$	Favre-filtered forward reaction rate constant of the i^{th} reaction
L_k	number of reactions involving the k^{th} species
Le_t	sub-grid scale turbulent Lewis number
M	Mach number
N_i	number of species involved in the i^{th} reaction
$\bar{p}$	filtered pressure (Pa)
$\bar{p}_g$	filtered gauge pressure (Pa)
Pr_t	sub-grid scale turbulent Prandtl number
Q_i^{sgs}	sub-grid scale heat flux in the i^{th} direction ($J \cdot m^{-2} \cdot s^{-1}$)
$\bar{q}_i$	filtered heat flux in the i^{th} direction ($J \cdot m^{-2} \cdot s^{-1}$)
r	spatial coordinate in the radial direction (m)
$\tilde{T}$	Favre-filtered temperature (K)
t	physical time (s)
$\tilde{U}_{k,j}$	Favre-filtered diffusion velocity component of k^{th} species in j^{th} direction ($m \cdot s^{-1}$)
$\tilde{u}$	Favre-filtered velocity component in the 1^{st} direction ($m \cdot s^{-1}$)
$\tilde{u}_i$	Favre-filtered velocity component in the i^{th} direction ($m \cdot s^{-1}$)
$\tilde{v}$	Favre-filtered velocity component in the 2^{nd} direction ($m \cdot s^{-1}$)
$\tilde{w}$	Favre-filtered velocity component in the 3^{rd} direction ($m \cdot s^{-1}$)
W_k	molecular weight of the k^{th} species ($kg \cdot mol^{-1}$)
x	spatial coordinate in the axial direction (m)
x_i	spatial coordinate in the i^{th} direction (m)
$\tilde{Y}_k$	Favre-filtered mass fraction of the k^{th} species
$\tilde{Z}$	Favre-filtered mixture fraction
δ_{ij}	Kronecker delta function
λ_{eff}	effective thermal conductivity ($W \cdot m^{-1} \cdot K^{-1}$)

μ_t	sub-grid scale turbulent viscosity ($Pa \cdot s$)
ν'_{ki}	reactant stoichiometric coefficient of the k^{th} species in the i^{th} reaction
ν''_{ki}	product stoichiometric coefficient of the k^{th} species in the i^{th} reaction
$\bar{\rho}$	filtered density ($kg \cdot m^{-3}$)
σ_i^{sgs}	sub-grid scale viscous work in the i^{th} direction ($J \cdot m^{-2} \cdot s^{-1}$)
τ	pseudo time (s)
$\tilde{\tau}_{ij}$	Favre-filtered stress tensor (Pa)
τ_{ij}^{sgs}	sub-grid scale stress tensor (Pa)
$\Phi_{k,j}^{sgs}$	sub-grid scale species flux of the k^{th} species in the j^{th} direction ($kg \cdot m^{-2} \cdot s^{-1}$)
	equivalence ratio
$\tilde{\chi}_j$	Favre-filtered mole fraction of the j^{th} species
$\overline{\dot{\omega}}_C$	filtered net mass production rate of progress variable ($kg \cdot m^{-3} \cdot s^{-1}$)
$\overline{\dot{\omega}}_k$	filtered net mass production rate of the k^{th} species ($kg \cdot m^{-3} \cdot s^{-1}$)

Funding

This work was funded partly by the Air Force Office of Scientific Research [Grant FA9550-18-1-0216], partly by NASA Grant NNX15AU96A, and partly by the William R.T. Oakes Endowment of the Georgia Institute of Technology.

ORCID

Suo Yang http://orcid.org/0000-0002-9924-2645

References

Barlow, R. S., and J. H. Frank. 1998. Effects of turbulence on species mass fractions in methane/air jet flames. *Symposium (International) on Combustion*, 27, 1087–95. doi:10.1016/S0082-0784(98)80510-9

Bilger, R. 1993. Conditional moment closure for turbulent reacting flow. *Phys. Fluids* 5:436–44. doi:10.1063/1.858867.

Bussing, T. R., and E. M. Murman. 1988. Finite-volume method for the calculation of compressible chemically reacting flows. *AIAA J.* 26:1070–78. doi:10.2514/3.10013.

Chen, T., S. Yang, A. C. Rousso, B. M. Goldberg, S. Wu, E. Kolemen, and Y. Ju. 2019. *Time-resolved electron temperature and species measurements and predictions of plasma-assisted reforming of methane. AIAA Scitech 2019 Forum*. San Diego, California: AIAA 2019–0465. doi:10.2514/6.2019-0465

Esclapez, L., P. C. Ma, E. Mayhew, R. Xu, S. Stouffer, T. Lee, H. Wang, and M. Ihme. 2017. Fuel effects on lean blow-out in a realistic gas turbine combustor. *Combust. Flame* 181:82–99. doi:10.1016/j.combustflame.2017.02.035.

Gao, X., S. Yang, and W. Sun. 2016. A global pathway selection algorithm for the reduction of detailed chemical kinetic mechanisms. *Combust. Flame* 167:238–47. doi:10.1016/j.combustflame.2016.02.007.

Gonzalez, E., A. Dasgupta, S. Arshad, and M. Oevermann 2017. Effect of the turbulence modeling in large-eddy simulations of nonpremixed flames undergoing extinction and reignition. *55th AIAA Aerospace Sciences Meeting*. Grapevine, Texas, AIAA 2017–0604. doi:10.2514/6.2017-0604

Han, W., V. Raman, and Z. Chen. 2016. Les/pdf modeling of autoignition in a lifted turbulent flame: Analysis of flame sensitivity to differential diffusion and scalar mixing time-scale. *Combust. Flame* 171:69–86. doi:10.1016/j.combustflame.2016.05.027.

Hsieh, S.-Y., and V. Yang. 1997. A preconditioned flux-differencing scheme for chemically reacting flows at all mach numbers. *Int. J. Comput. Fluid Dyn.* 8:31–49. doi:10.1080/10618569708940794.

Huo, H., and V. Yang. 2017. Large-eddy simulation of supercritical combustion: Model validation against gaseous H2-O2 injector. *J. Propul. Power* 33:1272–84. doi:10.2514/1.B36368.

Ihme, M., and H. Pitsch. 2008. Prediction of extinction and reignition in nonpremixed turbulent flames using a flamelet/progress variable model: 2. Application in LES of Sandia flames Dand E. *Combust. Flame* 155:90–107. doi:10.1016/j.combustflame.2008.04.015.

Jones, W., and V. Prasad. 2010. Large eddy simulation of the Sandia flame series (D–F) using the eulerian stochastic field method. *Combust. Flame* 157:1621–36. doi:10.1016/j.combustflame.2010.05.010.

Ju, Y., J. K. Lefkowitz, C. B. Reuter, S. H. Won, X. Yang, S. Yang, W. Sun, Z. Jiang, and Q. Chen. 2016. Plasma assisted low temperature combustion. *Plasma Chem. Plasma Process.* 36:85–105. doi:10.1007/s11090-015-9657-2.

Katta, V. R., and W. M. Roquemore. 2008. Calculation of multidimensional flames using large chemical kinetics. *AIAA J.* 46:1640–50. doi:10.2514/1.33131.

Legier, J.-P., T. Poinsot, and D. Veynante 2000. Dynamically thickened flame les model for premixed and non-premixed turbulent combustion. *Proceedings of the Summer Program, Center for Turbulence Research*. Stanford, California, 157–68.

Lew, J. K., S. Yang, and M. E. Mueller. 2017. Evaluation of a strain-sensitive transport model in LES of turbulent nonpremixed sooting flames. *Bull. Am. Phys. Soc. Division of Fluid Dynamics Meeting*. Denver, Colorado, F2.008.

Li, J., Y. Xia, A. S. Morgans, and X. Han. 2017. Numerical prediction of combustion instability limit cycle oscillations for a combustor with a long flame. *Combust. Flame* 185:28–43. doi:10.1016/j.combustflame.2017.06.018.

Lysenko, D. A., I. S. Ertesvåg, and K. E. Rian. 2014. Numerical simulations of the Sandia flame Dusing the eddy dissipation concept. *Flow Turbul. Combust.* 93:665–87. doi:10.1007/s10494-014-9561-5.

Marzouk, O. A., and E. D. Huckaby. 2010. A comparative study of eight finite-rate chemistry kinetics for CO/H2 combustion. *Eng. Appl. Comput. Fluid Mech.* 4:331–56. doi:10.1080/19942060.2010.11015322.

Meng, H., and V. Yang. 2003. A unified treatment of general fluid thermodynamics and its application to a preconditioning scheme. *J. Comput. Phys.* 189:277–304. doi:10.1016/S0021-9991(03)00211-0.

Menon, S., and A. R. Kerstein. 2011. The linear-eddy model. In Echekki, T., and E. Mastorakos (Eds.). *Turbulent combustion modeling* (pp. 221–247). Netherlands: Springer.

Moin, P., K. Squires, W. Cabot, and S. Lee. 1991. A dynamic subgrid-scale model for compressible turbulence and scalar transport. *Phys. Fluids* 3:2746–57. doi:10.1063/1.858164.

Peters, N. 1984. Laminar diffusion flamelet models in non-premixed turbulent combustion. *Prog. Energy Combust. Sci.* 10:319–39. doi:10.1016/0360-1285(84)90114-X.

Pierce, C. D., and P. Moin. 2004. Progress-variable approach for large-eddy simulation of non-premixed turbulent combustion. *J. Fluid Mech.* 504:73–97. doi:10.1017/S0022112004008213.

Pitsch, H., and H. Steiner. 2000a. Large-eddy simulation of a turbulent piloted methane/air diffusion flame (Sandia flame D). *Physics of Fluids (1994-present)* 12:2541–54. doi:10.1063/1.1288493.

Pitsch, H., and H. Steiner. 2000b. Scalar mixing and dissipation rate in large-eddy simulations of non-premixed turbulent combustion. *Proc. Combust. Inst.* 28:41–49. doi:10.1016/S0082-0784(00)80193-9.

Pope, S. B. 1985. PDF methods for turbulent reactive flows. *Prog. Energy Combust. Sci.* 11:119–92. doi:10.1016/0360-1285(85)90002-4.

Potturi, A., and J. R. Edwards 2013. Investigation of subgrid closure models for finite-rate scramjet combustion. *43rd Fluid Dynamics Conference*. San Diego, California, AIAA 2013–2461. doi:10.2514/6.2013-2461

Raman, V., and H. Pitsch. 2007. A consistent les/filtered-density function formulation for the simulation of turbulent flames with detailed chemistry. *Proc. Combust. Inst.* 31:1711–19. doi:10.1016/j.proci.2006.07.152.

Rousso, A., S. Yang, J. Lefkowitz, W. Sun, and Y. Ju. 2017. Low temperature oxidation and pyrolysis of n-heptane in nanosecond-pulsed plasma discharges. *Proc. Combust. Inst.* 36:4105–12. doi:10.1016/j.proci.2016.08.084.

Smagorinsky, J. 1963. General circulation experiments with the primitive equations: I. The basic experiment. *Mon. Weather Rev.* 91:99–164. doi:10.1175/1520-0493(1963)091<0099:GCEWTP>2.3.CO;2.

Smith, G. P., D. M. Golden, M. Frenklach, N. W. Moriarty, B. Eiteneer, M. Goldenberg, C. T. Bowman, R. K. Hanson, S. Song, W. C. Gardiner Jr., et al. *Gri-mech 3.0* [Online]. Available: http://www.me.berkeley.edu/gri_mech// [Accessed 2016].

Sun, W., X. Gou, H. A. El-Asrag, Z. Chen, and Y. Ju. 2015. Multi-timescale and correlated dynamic adaptive chemistry modeling of ignition and flame propagation using a real jet fuel surrogate model. *Combust. Flame* 162:1530–39. doi:10.1016/j.combustflame.2014.11.017.

Unnikrishnan, U., X. Wang, S. Yang, and V. Yang 2017. Subgrid scale modeling of the equation of state for turbulent flows under supercritical conditions. *53rd AIAA/SAE/ASEE Joint Propulsion Conference*. Atlanta, Georgia, AIAA 2017–4855. doi:10.2514/6.2017-4855

Wang, H. 2016. Consistent flamelet modeling of differential molecular diffusion for turbulent non-premixed flames. *Phys. Fluids* 28:035102. doi:10.1063/1.4942514.

Yang, S. 2017. *Effects of detailed finite rate chemistry in turbulent combustion*. Ph.D., Georgia Institute of Technology.

Yang, S., J. K. Lew, and M. E. Mueller. 2019a. Large eddy simulation of soot evolution in turbulent reacting flows: Presumed subfilter pdf model for soot–turbulence–chemistry interactions. *Combust. Flame* 209:200–13. doi:10.1016/j.combustflame.2019.07.040.

Yang, S., R. Ranjan, V. Yang, S. Menon, and W. Sun. 2017b. Parallel on-the-fly adaptive kinetics in direct numerical simulation of turbulent premixed flame. *Proc. Combust. Inst.* 36:2025–32. doi:10.1016/j.proci.2016.07.021.

Yang, S., R. Ranjan, V. Yang, W. Sun, and S. Menon. 2017c. Sensitivity of predictions to chemical kinetics models in a temporally evolving turbulent non-premixed flame. *Combust. Flame* 183:224–41. doi:10.1016/j.combustflame.2017.05.016.

Yang, S., S. Nagaraja, W. Sun, and V. Yang 2015. A detailed comparison of thermal and nanosecond plasma assisted ignition of hydrogen-air mixtures. *53rd AIAA Aerospace Sciences Meeting*. Kissimmee, Florida, AIAA 2015–1615. doi:10.2514/6.2015-1615

Yang, S., S. Nagaraja, W. Sun, and V. Yang. 2017a. Multiscale modeling and general theory of non-equilibrium plasma-assisted ignition and combustion. *J. Phys. D: Appl. Phys.* 50:433001. doi:10.1088/1361-6463/aa87ee.

Yang, S., V. Yang, W. Sun, S. Nagaraja, W. Sun, Y. Ju, and X. Gou 2016b. Parallel on-the-fly adaptive kinetics for non-equilibrium plasma discharges of C_2H_4/O_2/Ar mixture. *54th AIAA Aerospace Sciences Meeting*. San Diego, California, AIAA 2016–195. doi:10.2514/6.2016-0195

Yang, S., X. Gao, V. Yang, W. Sun, S. Nagaraja, J. K. Lefkowitz, and Y. Ju. 2016a. Nanosecond pulsed plasma activated C_2H_4/O_2/Ar mixtures in a flow reactor. *J. Propul. Power* 32:1240–52. doi:10.2514/1.B36060.

Yang, S., X. Wang, H. Huo, W. Sun, and V. Yang. 2019b. An efficient finite-rate chemistry model for a preconditioned compressible flow solver and its comparison with the flamelet/progress--variable model. *Combust. Flame* 210:172–82. doi:10.1016/j.combustflame.2019.08.035.

Zhang, Y., S. Yang, V. Yang, and W. Sun 2017. Effects of non-equilibrium plasma discharge on ignition and ntc chemistry of DME/O_2/Ar mixtures: A numerical investigation. *53rd AIAA/SAE/ASEE Joint Propulsion Conference*. Atlanta, Georgia, AIAA 2017–4773. doi:10.2514/6.2017-4773

Zhao, H., J. Fu, F. M. Haas, and Y. Ju. 2017. Effect of prompt dissociation of formyl radical on 1, 3, 5-trioxane and CH_2 Olaminar flame speeds with CO_2 dilution at elevated pressure. *Combust. Flame* 183:253–60. doi:10.1016/j.combustflame.2017.05.005.

Zong, N., and V. Yang. 2007. An efficient preconditioning scheme for real-fluid mixtures using primitive pressure–temperature variables. *Int. J. Comput. Fluid Dyn.* 21:217–30. doi:10.1080/10618560701584373.